

Generation and Robustness of Quantum Entanglement in Spin Graphs

Jan Riegemeyer,^{1,2} Dan Wignall,¹ Marta P. Estarellas,³ Irene D'Amico,¹ and Timothy P. Spiller¹

¹*Department of Physics, University of York, York, YO10 5DD, United Kingdom*

²*Fachbereich Physik, Westfälische Wilhelms-Universität Münster, 48149 Münster, Germany*

³*National Institute of Informatics, 2-1-2 Hitotsubashi, Chiyoda-ku, Tokyo 101-8430, Japan*

(Dated: March 22, 2022)

Entanglement is a crucial resource for quantum information processing. Protocols to generate high fidelity entangled states on various hardware platforms are in demand. While spin chains have been extensively studied to generate entanglement, graph structures also have such potential. However, only a few classes of graphs have been explored for this specific task. In this paper, we apply a particular coupling scheme involving two different coupling strengths to a graph of two interconnected 2-dimensional hypercubes of P_3 such that it effectively contains three defects. We show how this structure allows generation of a Bell state whose fidelity depends on the chosen coupling ratio. We apply partitioned graph theory in order to reduce the dimension of the graph and show that, using a reduced graph or a reduced chain, we can still simulate the same protocol with identical dynamics. We investigate how fabrication errors affect the entanglement generation protocol and how the different equivalent structures are affected, finding that for some specific coupling ratios these are extremely robust.

I. INTRODUCTION

Quantum computers hold the promise of being one of the next major technological developments in the field of information technology [1–3]. Quantum phenomena, such as entanglement and superposition of states, provide quantum computers with the ability to potentially solve some hard computational problems and simulations in a more efficient way than their classical counterparts [4–7]. One of the main current technological limitations rely on the number of qubits that can be allocated in a single chip [8, 9]. A way to overcome this, is to connect the different chips or registers through a quantum bus [8, 10]. When these interconnections are relatively short, it is desirable to use the same physical platform and avoid using hybrid systems and the associated inter-conversion from and to different encoding degrees of freedom (e.g. states of light in optical links) [8, 9]. For that purpose, arrangements (chains or graphs) of solid-state qubits are good candidates for short-range communication [8–11]. In addition to their application as quantum buses, spin chains and graphs are also able to perform other quantum information processing tasks, such as the creation and distribution of an entangled state [12–14].

Direct physical communication of a quantum state is not the only way of transferring quantum information, and, e.g., the teleportation protocol proposed by Bennett [15] uses entanglement to communicate quantum information. Entanglement is also present in a wide range of applications, such as one-way quantum computer architectures [16, 17] or quantum key distribution [18–20]. Given that entanglement is an ubiquitous resource for many applications, a reliable way to generate distributed entangled states on demand is paramount.

In this paper, we explore the dynamics and entanglement generation capabilities of a spin graph of two interconnected 2-dimensional hypercubes of P_3 engineered to present an "ABC-coupling" configuration [14] by using

two couplings of different strengths for a given coupling ratio. We use the methods of graph partitioning from Refs. [21, 22] to simplify such graph into a quotient graph and a quotient linear chain. In Sect. II we explain in detail the spin chain model. We also present the structure of the spin graph under study, as well as the partitioning theory that allows its simplification and the measure used to assess the quality of entanglement (the entanglement of formation or EOF). In Sect. III we present our results. For different coupling ratios, we compare the values of EOF obtained in a short period of time (the quantity relevant for experiments in the case of short decoherence times) against the maximum EOF values over a larger time window. We then investigate the effects that fabrication errors have on the entanglement generation. We analyse both the effects of errors on the couplings between qubits (non-diagonal disorder), and of errors on the on-site qubits' energies (diagonal disorder). Finally, our conclusions are included in Sect. IV.

II. THE MODEL

A. The spin chain formalism

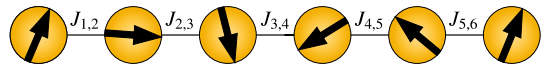


FIG. 1: Diagram of a spin chain of 6 qubits. $J_{i,i+1}$ are the coupling energies between two adjacent qubits. Tilted arrows pictorially represent superpositions of up and down spin states

A simple spin graph is the one-dimensional spin chain, an example of which is illustrated in Fig. 1. We describe such spin systems with the XY (sometimes also called XX) Heisenberg Hamiltonian. With $|0\rangle$ and $|1\rangle$ as our σ_z

basis states, we write the Hamiltonian as

$$H_{XY} = \sum_{i=1}^{N-1} J_{i,i+1} [|1\rangle\langle 0|_i \otimes |0\rangle\langle 1|_{i+1} + |0\rangle\langle 1|_i \otimes |1\rangle\langle 0|_{i+1}] + \sum_{i=1}^N \epsilon_i |1\rangle\langle 1|_i. \quad (1)$$

Note that throughout this paper we work in units where $\hbar = 1$. We will consider all the energies ϵ_i to be equal, time-independent and scaled to zero unless otherwise stated.

As already noted, some particular arrangements of spin chains or graphs present good quantum state transfer properties [8, 23–25], meaning that a quantum state can be reliably transmitted from a specific point of the graph (sender) to another (receiver).

B. Partitioned Graph Theory

We here consider the theory of graph partitioning based on [21], which allows reducing the complexity of a graph by collapsing several similar sites into a single vertex and readjusting the interaction strength. In [21], a partitioned graph G comprising a set of nodes, V_i , is defined such that:

- The first node V_1 comprises a single site.
- All sites collapsed in node V_i are equidistant from the first node V_1 .
- For any pair of nodes, i, j , every site in V_i connects to the same number of sites in V_j .
- No edges join sites in the same node.

Therefore we will group sites together in a node when they all have the same distance to the first node and the same coupling degree to sites in other nodes. Note that the distance between all pairs of connected sites is the same. So the distance between two sites is calculated by counting the number of connections that one has to pass when going from one site to the other.

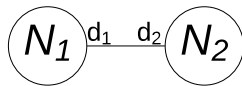


FIG. 2: Example of two nodes V_1 and V_2 connected to d_1 and d_2 sites, respectively. Node V_1 comprises N_1 sites and V_2 comprises N_2 sites [21]

In Fig. 2 we show two nodes V_1 and V_2 , where each site of the original graph in V_1 is coupled to d_1 sites in V_2 and each site in V_2 is coupled to d_2 sites in V_1 . It is always required that $N_1 d_1 = N_2 d_2$, or more generally

$$N_i d_i = N_j d_j \quad (2)$$

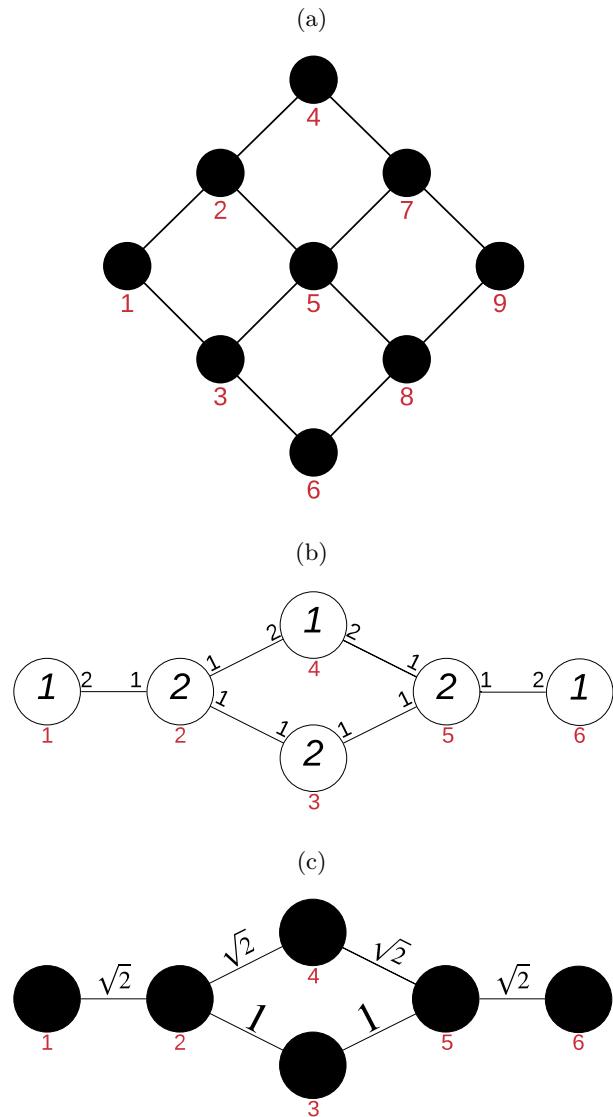


FIG. 3: The 2-dimensional hypercube of P_3 (a) together with the corresponding partitioned graph (b) and the quotient graph (c). The numbers on the connections in the partitioned graph describe the coupling degrees of the nodes and the numbers on the connections in the quotient graph denote the engineered coupling strengths, $J_{i,j}$. Note that for the original P_3 hypercube all coupling strengths $J_{i,j} = 1$. The red numbers at the bottom of each circle are labelling the sites of the graphs (a) and (c) and the nodes of the partitioned graph (b)

for any coupled pair of nodes i, j .

Once the partitioned graph is obtained, the quotient graph can be easily defined. The site structure of the quotient graph is identical to the node structure of the partitioned graph, however each site is now interacting with the adjacent sites through an effective coupling strength $J_{1,2} = \sqrt{d_1 d_2}$. The quotient graph presents the same dynamics, and therefore quantum transfer abilities, than the

original non-partitioned graph, in which all the vertices were uniformly coupled with $J = 1$. To avoid confusion, we will call the vertices of the original graph sites and the vertices of the quotient graph qg-sites.

The original P_3 hypercube together with the partitioned and quotient graph are represented in Fig. 3. We note that for the presented quotient graph, Bachmann et al. introduced a lift-and-quotient reduction [22], allowing for a further simplification of the graph. The top structure from Fig. 4 can be reduced to the graph at the bottom right using the aforementioned partitioned graph theory. We do, however, have some freedom in the way we perform that partition. If we only partition the grey coloured sub-graph at the top, we get the graph at the bottom left. The three graphs present the same dynamics if the original graph is initialized in a normalized equal superposition between the sites corresponding to the initially excited qg-site of the quotient graph.

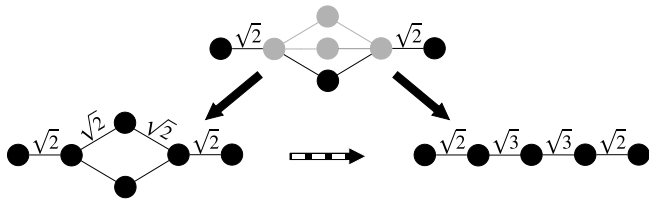


FIG. 4: Sketch of the lift-and-quotient reduction [22]

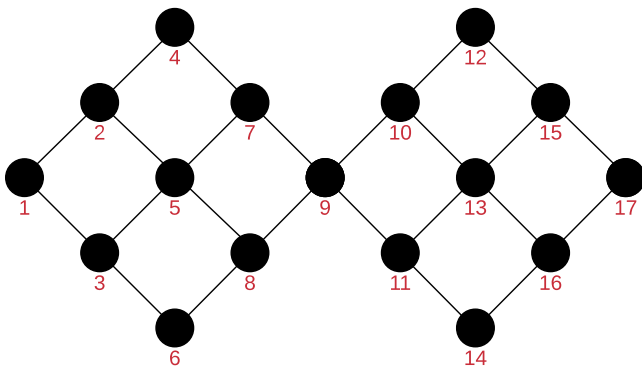


FIG. 5: Graph of two interconnected 2-dimensional hypercubes of P_3

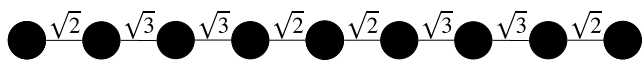


FIG. 6: Quotient linear chain for the two interconnected 2-dimensional hypercubes of P_3 from Fig. 5

Using the structure from Fig. 3a as our basic unit, we interconnect two of them in order to generate the structure that will be used in our entanglement generation protocol (see Fig. 5). If we apply the partitioning method and the lift-and-quotient reduction to the two coupled P_3 hypercubes from Fig. 5, we obtain a linear chain, as

shown in Fig. 6. We will call the vertices of this quotient linear chain lc-sites.

C. Unitary Transformation Perspective

An alternative and more physical perspective on the graph partition and quotient combined operation is to consider this operation as due to a unitary transformation. The reduction of the complexity of a graph to a simpler graph (with fewer coupled sites), or even a simple chain (with still fewer coupled sites), can be viewed as due to a unitary transformation. As we are considering the single excitation subspace of our system, the Hamiltonian has the same dimensionality as the site basis and the transformation redefines the definitions of (some of) the sites to superpositions of the original site basis. There are two criteria for the transformation. First, it should decouple some of the sites, to simplify the graph. Second, it should leave alone the definitions of the sites between which we seek identical dynamics in the reduced graph.

Clearly this perspective also works in reverse, in the sense that we could start with a simple graph or chain, and augment this with some additional uncoupled sites (which could be at zero energy or non-zero energy, dependent upon the form of the more complicated graph sought). Then a unitary transformation can be chosen to redefine the site basis and involve the uncoupled sites in a more complex graph. If in this reverse approach the objective is again a network with identical dynamics between certain sites, these sites should be invariant under the transformation.

In both cases (graph simplification and graph expansion) where the sites of interest for the dynamics are not invariant under the transformation, there are clearly still equivalent dynamics in the two graphs. However these will involve site superposition states, as related by the transformation.

We will refer to this unitary perspective in relation to the specific examples discussed in this paper.

D. ABC Configuration

We now extend what in [14] is called ABC configuration to our specific graph structure. This configuration is attained by imposing a coupling distribution of two different energies, Δ and δ , that results in having three sites (named A, B and C) distributed symmetrically and weakly coupled (δ) to the rest of the system, such that they appear to be defects in an otherwise strongly coupled (Δ) graph. The reason that makes this particular configuration interesting is that it can be approximated to a trimer chain, which has the ability to dynamically create maximally entangled Bell state between the edge sites when the system is initialised with a spin up in the middle site [14, 26]. Figure 7 shows the result of using this

configuration in our original graph and its two quotient structures.

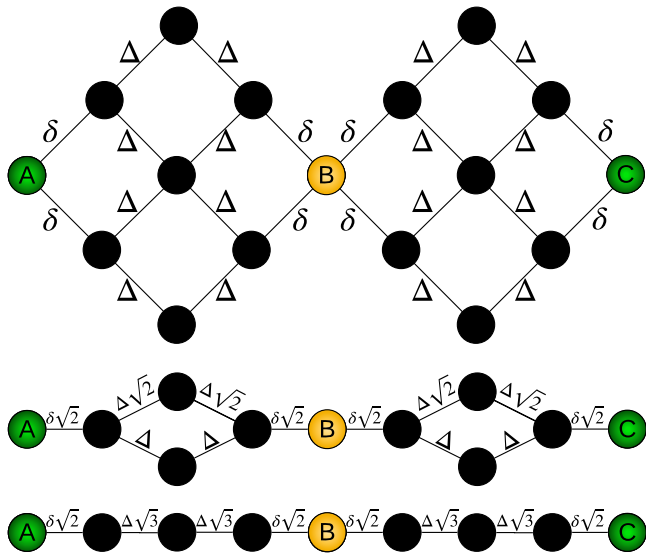


FIG. 7: ABC configuration of the original two interconnected P_3 hypercubes (top), the quotient graph (middle) and the quotient linear chain (bottom)

From the unitary transformation perspective, the ABC system has seventeen single-excitation eigenstates, with eigen-energies as given in Fig. 8. The first partition and quotient operation is effected by a transformation that acts only on the black sites in Fig. 7 and leaves A, B and C invariant. This decouples six sites (two at positive energy $\sqrt{2}\Delta$, two at equal magnitude negative energy $-\sqrt{2}\Delta$ and two at zero energy), clearly without changing the overall spectrum of the system. The resultant non-trivial network is the 11-site quotient graph shown. A further unitary transformation, again acting on only the black sites and leaving A, B and C invariant, can decouple a further two zero energy sites to leave the final 9-site chain, with the spectrum given in Fig. 8.

E. Entanglement-of-formation as a measure of graph performance

To determine the effectiveness of any particular spin chain or graph to generate entangled states, a quantitative measurement of bipartite entanglement is needed. For this, we will use the entanglement of formation (EOF) [27]. The EOF between qubits A, C is defined by,

$$EOF_{AC} = -x \log_2 x - (1-x) \log_2 (1-x), \quad (3)$$

where $x = \frac{1+\sqrt{1-\tau}}{2}$ and $\tau = (\max\{0, \lambda_1 - \lambda_2 - \lambda_3 - \lambda_4\})^2$. λ_i is the square root of the i^{th} eigenvalue of the matrix $\rho_{AC}\widetilde{\rho_{AC}} = \rho_{AC}[(\sigma_y^A \otimes \sigma_y^C)\rho_{AC}^*(\sigma_y^A \otimes \sigma_y^C)]$, ordered such that $\lambda_1 > \lambda_2 > \lambda_3 > \lambda_4$. ρ_{AC} is the reduced density

Six eigen-energies that decouple in the reduction from 17-site to 11-site	$\sqrt{2}\Delta, \sqrt{2}\Delta$ $-\sqrt{2}\Delta, -\sqrt{2}\Delta$ $0, 0$
Two eigen-energies that decouple in the reduction from 11-site to 9-site	$0, 0$
Nine eigen-energies that remain in the 9-site quotient linear chain	$\pm\sqrt{3\delta^2 + 3\Delta^2 \pm \sqrt{\delta^4 + 9\Delta^4}}$ $\pm\sqrt{\delta^2 + 3\Delta^2 \pm \sqrt{\delta^4 + 9\Delta^4}}$ 0

FIG. 8: The seventeen single-excitation eigen-energies of the network shown in Fig. 7, identifying those that decouple with the reductions

matrix for sites A and C that result from tracing out the rest of the system, such that $\rho_{AC} = \text{tr}_{rest}(\rho)$.

The EOF ranges between 0 and 1, with $EOF = 1$ indicating that the state comprising two qubits is maximally entangled.

III. RESULTS

In order to assess the amount of entanglement generated by the graphs, we simulate the dynamics of the system. Note that, as already mentioned, the three structures (original graph, quotient graph and quotient chain) will have the same dynamics for injection and collection at sites A, B, and C. For that, we initialise the system to a spin up, $|1\rangle$, at site B and all spins down, $|0\rangle$, in the rest of the graph. We then let the state evolve through its natural dynamics and calculate the EOF versus time. Because we based our structure on the trimer chain, the dynamics of the EOF will look like a Rabi oscillation that corresponds to the entangling and disentangling of the state comprising sites A and C. In the remaining of this section we study in detail how the amplitude and period of such oscillations depend on the chosen coupling ratio, $\frac{\delta}{\Delta}$, and how such ratio affects the time one needs to wait to obtain the maximum EOF peak. We also study how the presence of random fabrication errors (diagonal and off-diagonal disorder) affects differently the dynamics of the three graph structures, giving different results in terms of robustness.

A. Entanglement generation

In Fig. 9 we show the EOF dynamics for two different coupling ratios, $\frac{\delta}{\Delta} = 0.1$ and $\frac{\delta}{\Delta} = 1$. The peaks for each of the two scenarios present different periodicity and

relative amplitudes. In Fig. 9 it is also apparent that the larger the coupling ratio, the faster the oscillations, meaning that the entangled state is generated earlier. For $\frac{\delta}{\Delta} = 1$, the first *EOF* peak happens at $t_1 \cdot \Delta = 1.97$ and for $\frac{\delta}{\Delta} = 0.1$, at a time $t_1 \cdot \Delta = 18.02$.

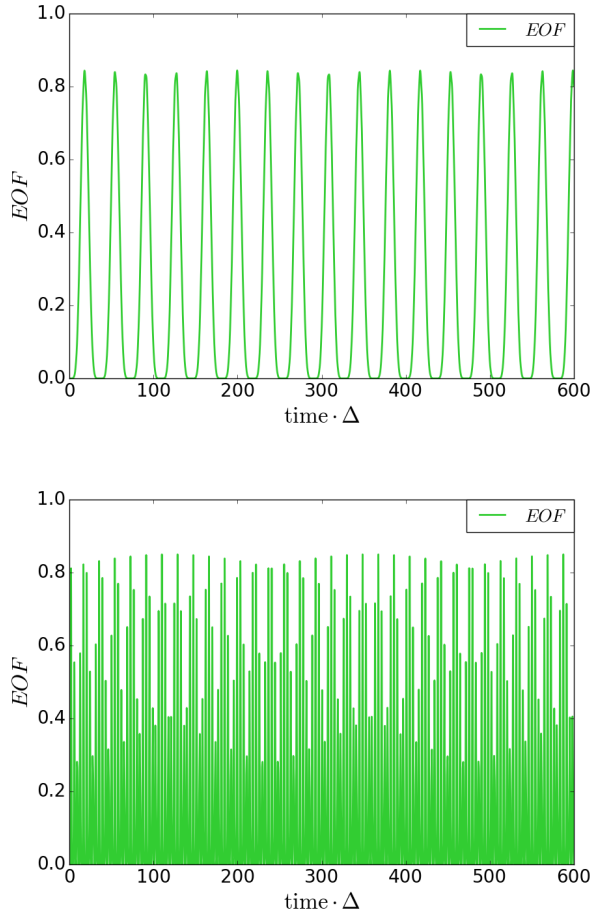


FIG. 9: Dynamics of the *EOF* between sites A and C with a coupling ratio $\frac{\delta}{\Delta} = 0.1$ (top) and $\frac{\delta}{\Delta} = 1$ (bottom). A coupling ratio of $\frac{\delta}{\Delta} = 1$ corresponds to the case with uniform couplings

1. *EOF* at the first peak

Our first approach to compare the effect of the different coupling ratios in our protocol is to investigate the first *EOF* peak. From an experimental point of view, the evaluation of the first peak is a useful metric as it will be most likely to fall ahead of the decoherence times of the experimental realisation. The dependence of the time when the first entanglement operation happens can be analytically approximated from the reduced trimer as

done in [26]. From that, we get

$$t_P \cdot \Delta = \frac{\pi}{\sqrt{3 + \left(\frac{\delta}{\Delta}\right)^2} - \sqrt{9 + \left(\frac{\delta}{\Delta}\right)^4}} \quad (4)$$

as the estimate of the period of the *EOF* oscillation and of the time needed for an excitation injected at site B to propagate to the edges and come back to its initial state. Thus, the entangled state will be formed for the first time at approximately $t_P \cdot \Delta/2$.

The coupling ratio dependence of the first *EOF* peak t_1 for the two interconnected 2-dimensional hypercubes of P_3 is shown by the orange curve in Fig. 10, and it is identical for the three structures (original graph, quotient graph and quotient chain). The value of this peak shows an oscillatory behaviour, with low amplitude, fast oscillations at small coupling ratios, and high amplitude, slow oscillations at larger coupling ratios. We observe that the highest *EOF* attained is $EOF = 0.8745$ for a coupling ratio of $\frac{\delta}{\Delta} = 0.82846$. In the right inset of Fig. 10 we show how the time t_1 decays as the coupling ratio increases, a result that is in agreement with the analytical approach. The dependence of t_1 on the coupling ratio has a staircase-like profile; these quick vertical drops occur at the ratios corresponding to the minima of the orange dashed curve in the main panel. This behaviour can be understood if we look at a few consecutive slices of the dynamics for the region close to those minima. Figure 11 shows three nearby points to the minimum close to $\frac{\delta}{\Delta} = 0.5$. From the lower $\frac{\delta}{\Delta}$ to the higher, we observe how the *EOF* curve goes from having a clear maximum to reach a plateau, and then the maximum can be distinguished again. This transition results in a t_1 step (note how the maximum that was initially at the right-hand side appears at the left side after reaching the flat plateau), as seen in the right inset in Fig. 10. This behaviour can be observed at all of the minima of the orange dashed curve in Fig. 10.

2. Comparison to "normal" linear chain

If we are changing the coupling ratio of the quotient linear chain in Fig. 7 from $\sqrt{2}\delta/\sqrt{3}\Delta$ to δ/Δ we find that the plot is the same with a rescaled factor $\sqrt{3}/\sqrt{2}$. So if one has only two specific couplings δ and Δ available due to experimental constraints, then using the full graph generates faster dynamics (a shorter t_1) than a coupled linear chain generated by those two couplings. The dynamics of the full graph is equivalent to the dynamics of an 'enhanced' spin chain with coupling boosted by a factor $\sqrt{3}/\sqrt{2}$.

3. Entanglement within a Longer Time

A different approach to compare the coupling ratio dependence is to use the maximum entanglement generated

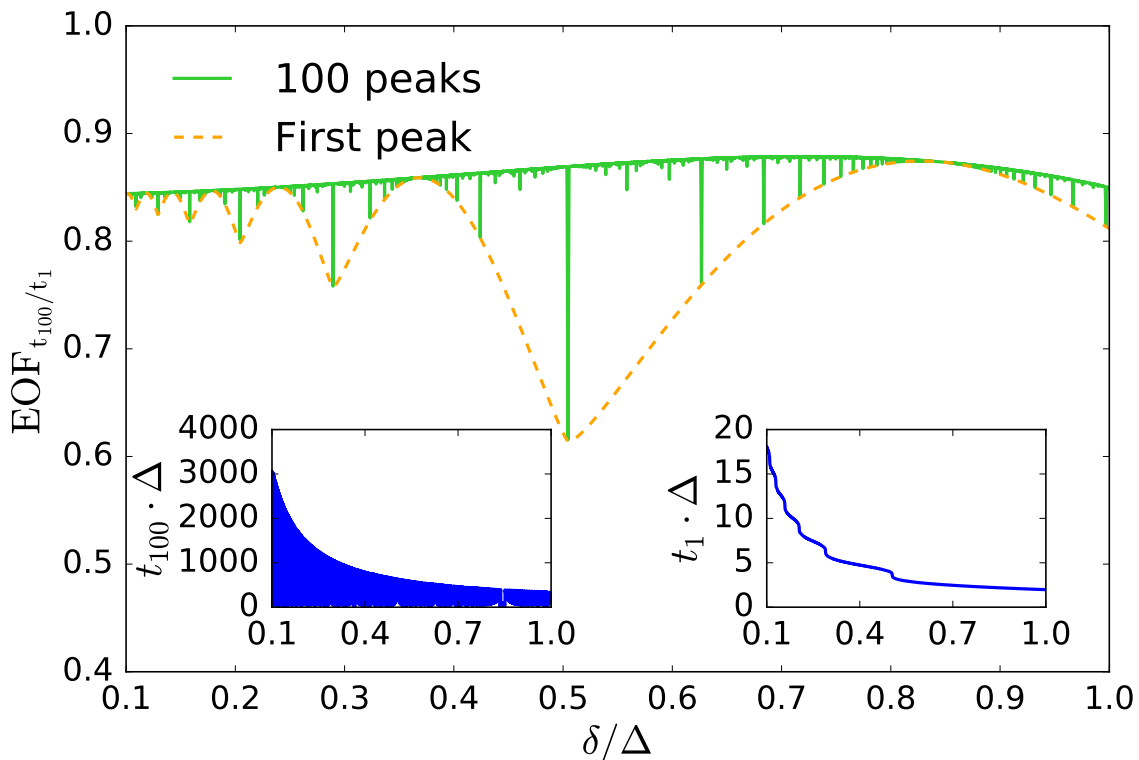


FIG. 10: Orange dashed Curve: EOF at t_1 plotted against the coupling ratio $\frac{\delta}{\Delta}$. This value is obtained as the highest entanglement found in a time window of t_P . Green solid Curve: Maximum EOF in a time window of $100 \cdot t_P$ against the coupling ratio $\frac{\delta}{\Delta}$. In the left inset, the time t_{100} when the maximal entanglement within $100 \cdot t_P$ occurs is plotted against the coupling ratio. In the right inset, the time t_1 when the first entanglement peak occurs is plotted against the coupling ratio

over a larger time window. In this section, we look at the maximum EOF in a time window equal to 100 periods, $t = 100 \cdot t_P$ (note that t_P will depend on the coupling ratio). We denote t_{100} the time at which the highest entanglement $EOF_{t_{100}}$ in the time of 100 trimer periods occurs. Figure 10 shows the dependence of the maximum EOF (green solid profile) with the coupling ratio. For this scenario and a coupling ratio of $\delta/\Delta = 0.72018$ we get the highest maximum entanglement, $EOF = 0.8787$. The left-hand inset in Fig. 10 shows the time t_{100} when the maximal entanglement occurs. The upper limit is given by the time window $t = 100 \cdot t_P$ and is decreasing with the coupling ratio. One can see that the maximal entanglement occurs at various times within the time window. We will later have a more detailed look at this time behaviour.

The green solid line in Fig. 10 outlines an upper limit with respect the orange dashed curve, but it also displays a few downward outliers. For such cases, the highest possible entanglement occurs at a time out of the selected time frame due to the presence of secondary oscillations of a large period (examples of secondary oscillations can be seen in Fig. 9). We will call these outliers ‘downwards peaks’. Note, that the ‘downwards peaks’ are very sharp so we need a high precision in the coupling ratio to iden-

tify them. The sharpness of the ‘downwards peaks’ also underlines the quick change in the secondary oscillations just by slightly modifying the coupling ratio.

4. Ratios for perfect periodicity

In Fig. 10, for certain ratios, the green solid curve shows ‘downwards peaks’ touching the orange dashed curve; this behaviour implies that that no EOF -peak is higher than the first peak in the specified time frame of $100 \cdot t_P$. However, many of these downward peaks remain when considering an arbitrarily large time window, suggesting that no EOF peak is higher than the first peak. This either means that the first EOF peak is highest, or that all EOF peaks are the same height. We shall see through inspection of one of these ‘downward peaks’ that the latter is true.

As shown in Fig. 12, the state of the system at those specific coupling ratios is fully periodic. Hence, the system returns exactly to its initial state before the second EOF peak which must therefore be the same shape as the first. We conclude that all the peaks are the same for the specific coupling ratios showing ‘downwards peaks’.

There are multiple ratios for which this is true, the

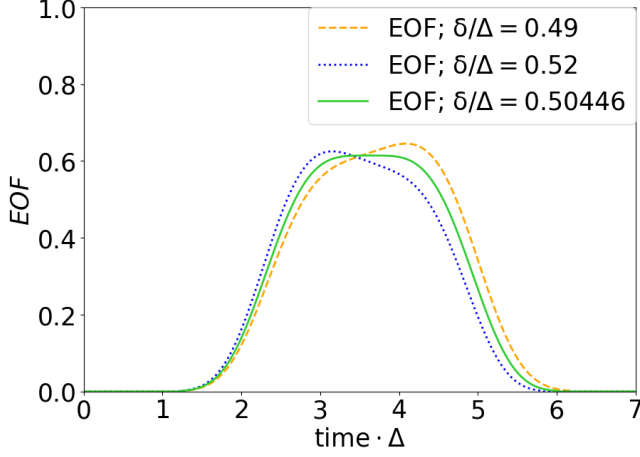


FIG. 11: *EOF* for ratios around the orange dashed curve minimum near $\frac{\delta}{\Delta} = 0.50446$ in Fig. 10. The shifting of the maximum from the right hand side of the peak to the left hand side explains the staircase like profile of the left inset in Fig. 10. Orange dashed: *EOF* vs. time for a coupling ratio slightly smaller than the rightmost minimum of the orange dashed curve in Fig. 10. Green solid: *EOF* vs. time for a coupling ratio equal to the rightmost minimum of the orange dashed curve in Fig. 10. Blue dotted: *EOF* vs. time for a coupling ratio slightly larger than the rightmost minimum of the orange dashed curve in Fig. 10

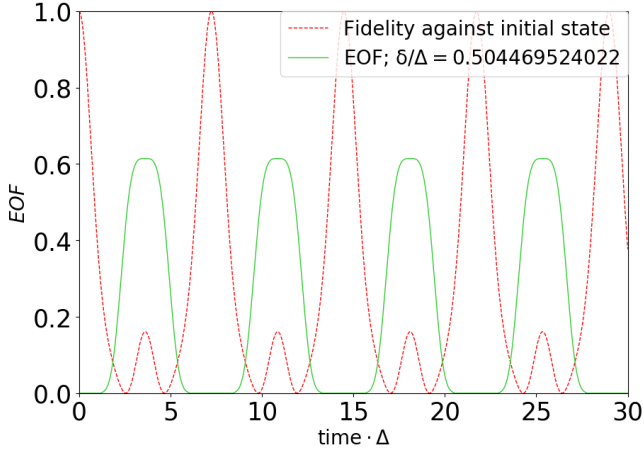


FIG. 12: *EOF* (green solid) at the coupling ratio of one of the ‘downwards peaks’ (the rightmost minimum of the orange dashed curve in Fig. 10) and the fidelity against the initial state (red dashed) showing that the system returns periodically to its initial state

reason for this, and the precise values of these ratios, can be discovered through analysis of the fidelity against the initial state.

For an initial state $|\psi_0\rangle$, the fidelity against a state $|\psi_f\rangle$,

is defined as

$$\mathcal{F}(t) = |\langle \psi_f | e^{-it\mathcal{H}} | \psi_0 \rangle|^2 \quad (5)$$

where \mathcal{H} is the time-independent systems Hamiltonian. By diagonalising \mathcal{H} , which has eigenvalues and eigenvectors $\{E_i\}$ and $\{|\phi_i\rangle\}$, the fidelity can be written as

$$\mathcal{F}(t) = \sum_{i,j} \alpha_{ij} e^{it(E_j - E_i)}. \quad (6)$$

Where we have defined $\alpha_{ij} = \langle \phi_j | \psi_f \rangle \langle \psi_f | \phi_i \rangle \langle \phi_i | \psi_0 \rangle \langle \psi_0 | \phi_j \rangle$. By noting that $\alpha_{ij} = \alpha_{ji}^*$, and $e^{it(E_j - E_i)} = (e^{it(E_i - E_j)})^*$, we can see that the imaginary part of the i, j term cancels with the imaginary part of the j, i term therefore, as the diagonal terms, $\alpha_{ii} e^{it(E_i - E_i)}$ are real, the fidelity can be written as a sum of cosines:

$$\mathcal{F}(t) = \sum_{i,j} \alpha_{ij} \cos((E_j - E_i)t). \quad (7)$$

As the dynamics we are interested in are the same between the full, seventeen vertex graph, the quotient graph and the quotient chain, for simplicity we shall analyse this for the case of the quotient linear chain (with an initial injection in the centre lc-site B). For this system, there are nine eigenvectors, five even under reflection about lc-site B and four odd under this reflection. There are thus five eigenvectors which are not orthogonal to the (even) initial state, and therefore affect $\mathcal{F}(t)$. These eigenvectors have the corresponding energies, taken from Fig. 8 and defined as:

$$\pm E := \pm \sqrt{3\delta^2 + 3\Delta^2 + \sqrt{\delta^4 + 9\Delta^4}} \quad (8)$$

$$\pm E' := \pm \sqrt{3\delta^2 + 3\Delta^2 - \sqrt{\delta^4 + 9\Delta^4}} \quad (9)$$

$$E_0 := 0. \quad (10)$$

As $\alpha_{ij} = 0$ when either $|\varphi_i\rangle$ or $|\varphi_j\rangle$ is orthogonal to the initial state $|\psi_0\rangle$, these are the only eigenvalues that affect the time dependence of $\mathcal{F}(t)$. By considering all combinations of these five eigenvalues in the term $\cos((E_j - E_i)t)$, and noting that cosine is an even function, it can be shown that for all the cosines in the sum to equal unity (and therefore for the fidelity to return to its initial state) the following must be satisfied:

$$Et = 2\pi n_1$$

$$E't = 2\pi n_2$$

$$2Et = 2\pi n_3$$

$$2E't = 2\pi n_4$$

$$2(E - E')t = 2\pi n_5$$

$$2(E + E')t = 2\pi n_6$$

for some integers n_i . Of course these equations are not independent, if the first two are satisfied, then so are the rest. Therefore, when $E'n_1 = En_2$, $\mathcal{F}(t) = 1$ at time $t = \frac{2\pi n_1}{E} = \frac{2\pi n_2}{E'}$.

Using this integer condition, and the formulae for the energies, we can derive a formula which will tell us, for a given n_1, n_2 , what coupling ratio ensures that the condition $E'n_1 = En_2$ is true. When $n_2 = 1$, the formula results in all the ratios such as the one in Fig. 12, where all the large peaks in fidelity are equal to unity. The ratio shown in Fig. 12, $\frac{\delta}{\Delta} = 0.504469524022$, is produced when $n_2 = 1$ and $n_1 = 3$.

5. Time Behaviour around "Flat Coupling Ratios"

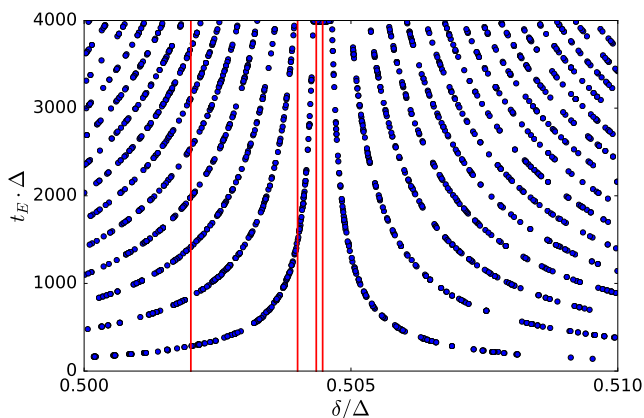


FIG. 13: Time behaviour around the coupling ratio displaying a minimum of the orange dashed curve in Fig. 10. Every point stands for the time when the highest EOF is observed in a time window of $t \cdot \Delta = 4000$. To be sure that the shape which can be seen is not due to the sampling of the coupling ratios, we have chosen 2000 random coupling ratios in the range $[0.50, 0.51]$. Due to the fact that our EOF against time plots consist of many single data points, always one time point shows an EOF a bit larger than the other points even though they are all of equal height. Hence, there are no continuous lines in the figure. Figure 15 in the appendix shows plots of EOF vs. time $\cdot \Delta$ for the vertical red lines

Here we consider coupling ratios within a small interval around the minimum of the orange dashed curve of Fig. 10 that give the downwards peaks for the green solid curve of Fig. 10. We investigate the time when the highest EOF occurs by considering a fixed time window. In Fig. 13 we show the highest EOF within the observed time $t \cdot \Delta = 4000$ for small variations of the coupling ratios around $\delta/\Delta = 0.505$. The period of the secondary oscillations becomes longer if we get closer to the minimum of the orange dashed curve in Fig. 10. Therefore, the number of the EOF -maxima from the secondary oscillations within the observed time window decreases. This

behaviour is confirmed in Fig. 13 since the number of blue curves which we can see in the time window intersecting the cut for a given $\frac{\delta}{\Delta}$ decreases as we get closer to the minimum coupling ratio (see also the appendix where we show the EOF against the time for the vertical lines in Fig. 13). Close to this coupling ratio, the highest EOF within the time window occurs just before $t \cdot \Delta = 4000$ and the absolute highest EOF (a maxima of the secondary oscillation) occurs outside the time window. As the coupling ratio approaches the minimum of the orange dashed curve in Fig. 10 the time when the absolute highest EOF occurs goes to infinity. Then we cannot see any secondary oscillations. We call all the coupling ratios which lead to an infinite long period of the secondary oscillations "flat coupling ratios".

B. Stability against errors: Random Static Disorder

So far we have discussed the behaviour of an ideal system, with no errors in the coupling strengths between sites and where all of the on-site energies are precisely equal and scaled to zero. This is of course an unrealistic situation and a consideration of how robust a system is to errors in manufacturing is critical to determining its practical feasibility. Following [28], to study our systems robustness we introduce two types of static disorder. The first, *diagonal disorder*, consists of adding random perturbations to the diagonal terms of the Hamiltonian, and represents random differences between the onsite energies of the qubits. The second type of disorder we apply, *off-diagonal disorder*, represents random errors in the couplings between qubits, and is incorporated into the simulation by adding random perturbations to the non-zero off-diagonal terms of the Hamiltonian. To see the effect of these errors on the dynamics of the system, we apply these perturbations to two different coupling scenarios: a coupling ratio of $\frac{\delta}{\Delta} = 0.828$ (corresponding to the rightmost maximum of the orange dashed curve in Fig. 10) and a coupling ratio of $\frac{\delta}{\Delta} = 0.109$ (corresponding to one of the left most minimum of the orange dashed curve in Fig. 10). We scale the errors via a disorder scale, D , ranging from 0% to 50% of Δ , which is added to the couplings or energies as a dimensionless parameter such that $\bar{\epsilon}_i = \epsilon_i + Dr_i\Delta$ and $\bar{J}_{i,i+1} = J_{i,i+1} + Dr_i\Delta$, where r_i is a random number obtained from a uniform distribution. For both types of added disorder we perform 1000 random realisations, and for each we obtain the EOF at the time of the first peak in the unperturbed system, t_1 , and then calculate the average.

In Fig. 14, we compare the robustness of the graph structure of Fig. 5 to its quotient graph and quotient linear chain. We find that even though the three graph structures show a quick decay of the averaged EOF for the coupling ratio $\frac{\delta}{\Delta} = 0.109$ (top panel), for the case of the coupling ratio $\frac{\delta}{\Delta} = 0.828$ we observe an excellent robustness (bottom panel), especially in the case of diag-

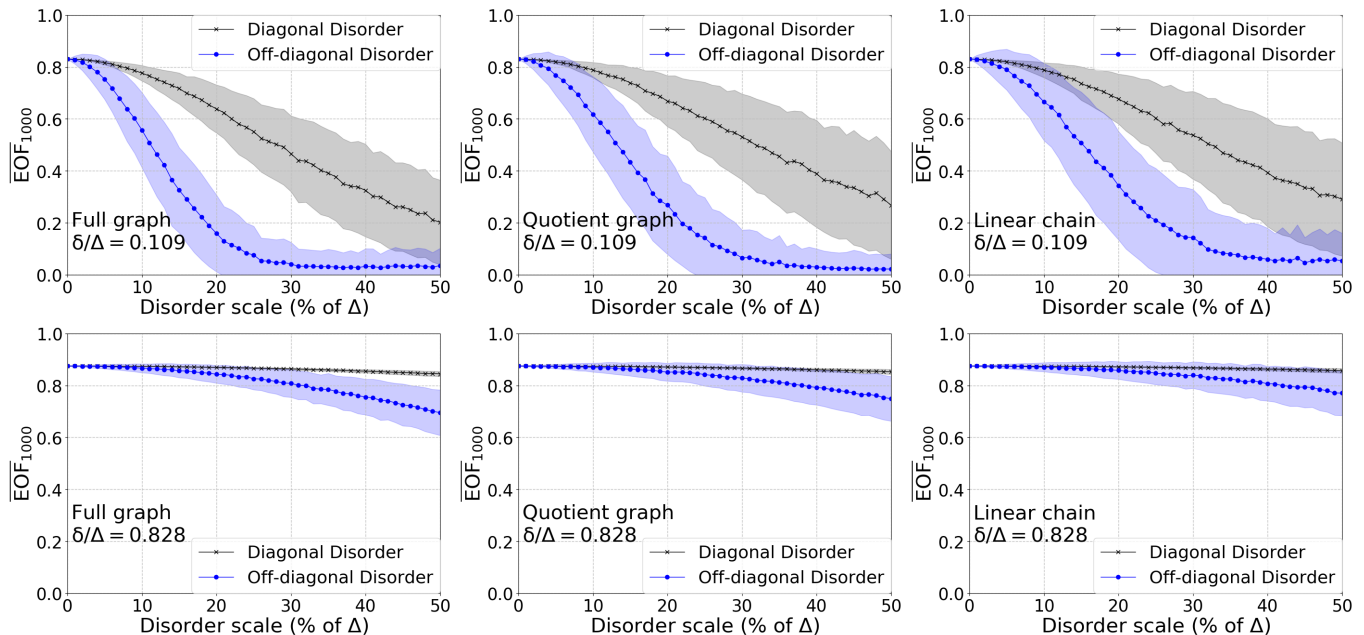


FIG. 14: Stability against disorder. *Top*: $\frac{\delta}{\Delta} = 0.109$; *Bottom*: $\frac{\delta}{\Delta} = 0.828$. *Left*: Full graph; *Middle*: Quotient graph; *Right*: linear chain. Off-diagonal disorder is shown in blue with dots, diagonal disorder is shown in black with crosses. The three graph structures display a very similar response to both disorders

onal disorder. Hence, there is a strong dependence on the robustness of our protocol with the chosen coupling ratio.

IV. CONCLUSIONS

Using a graph of two interconnected 2-dimensional P_3 hypercubes, we have shown that one can efficiently generate bipartite entanglement by preparing an initial state with an excitation in the middle vertex of the graph. We engineered the graph couplings with a strong and weak coupling distribution such that we obtain an ABC configuration that can be approximated to the trimer chain, known to generate Bell pairs. We analysed the spin dynamics dependent on the ratio of the weak and strong coupling and found specific coupling ratios where the entanglement shows a perfect periodic behaviour. This behaviour, however, can be rapidly lost only by a slight change on the coupling ratio. In such cases we encounter secondary oscillations causing the entanglement peaks to have a different height, and therefore showing a different EOF . For experimental implementations we suggest the coupling ratio $\frac{\delta}{\Delta} = 0.828$ since it leads to the highest entanglement of the first entanglement peak, and this occurs within a short time due to faster dynamics for higher coupling ratios.

We used graph partition theory to derive three related graphs, and showed that the above findings are identical for the three graphs. In addition, we discussed the partitioning from the physical perspective of unitary transformations applied to redefine some of the graph sites. All

three graphs depicted in Fig. 7 show the same dynamics after an excitation is injected in the middle. Moreover, the three graphs show the same dynamics if the initial state of the full graph is a normalized superposition between the sites which correspond to the initially excited qg-sites of the quotient graph and, in turn, the initially excited lc-sites of the quotient linear chain. This gives experimentalists flexibility in their system's topology e.g for certain hardware, a full graph could be more favorable to implement than a linear chain, or it could offer additional functionalities. In addition, if the set of available couplings is limited, the full graph is advantageous as it corresponds to a "boosted" spin chain.

Finally we considered the robustness of the three systems. We found that there is a significant dependence on the ratio $\frac{\delta}{\Delta}$, as the systems with a ratio $\frac{\delta}{\Delta} = 0.828$ are significantly more robust than the ones with ratio $\frac{\delta}{\Delta} = 0.109$. We also noted that errors affecting the coupling between sites ('off-diagonal disorder') are more damaging to the entanglement generation protocol than errors affecting the on-site energies of the sites ('diagonal disorder'). The three graph structures show similar robustness, although the linear chain is slightly more robust than the quotient graph which in turn is slightly more robust than the full graph. These results suggest that a physical realisation of the systems shown in Fig. 7 should aim for a ratio of $\frac{\delta}{\Delta} = 0.828$, as it not only produces a high EOF in a shorter time, but is also extremely robust.

We conclude that graph structures with only two different couplings δ and Δ can be used to generate robust bipartite entanglement. While a linear chain with

the same dynamics as the graph is slightly more robust to errors, a linear chain with the same coupling as the graph displays a slower dynamics. Experimental research is needed to weight between using graphs or chains for the design of different quantum technology applications, such as noisy intermediate-scale quantum chips and modular quantum computer architectures.

CONFLICT OF INTEREST

The authors declare that they have no conflict of interest.

ACKNOWLEDGEMENTS

J. Riegemeyer would like to thank J. Risske for helpful discussions about the code written to run the simulations.

-
- [1] M. A. Nielsen and I. Chuang, *Quantum Computation and Quantum Information* (Cambridge University Press, Cambridge, 2000).
- [2] D. Deutsch and R. Jozsa, Proc. R. Soc. Lond. A **439**, 553 (1992).
- [3] T. D. Ladd, F. Jelezko, R. Laflamme, Y. Nakamura, C. Monroe, and J. L. O'Brien, Nature **464**, 45 (2010).
- [4] P. W. Shor, SIAM Rev. **41**, 303 (1999).
- [5] F. Arute, K. Arya, R. Babbush, D. Bacon, J. C. Bardin, R. Barends, R. Biswas, S. Boixo, F. G. Brandao, D. A. Buell, *et al.*, Nature **574**, 505 (2019).
- [6] C. H. Bennett and D. P. DiVincenzo, Nature **404**, 247 (2000).
- [7] D. Bruss and G. Leuchs, *Lectures on quantum information* (Wiley-VCH, Hoboken, 2007).
- [8] S. Bose, Contemp. Phys. **48**, 13 (2007).
- [9] D. Kielpinski, C. Monroe, and D. J. Wineland, Nature **417**, 709 (2002).
- [10] A. Skinner, M. Davenport, and B. E. Kane, Phys. Rev. Lett. **90**, 087901 (2003).
- [11] J. G. Bohnet, B. C. Sawyer, J. W. Britton, M. L. Wall, A. M. Rey, M. Foss-Feig, and J. J. Bollinger, Science **352**, 1297 (2016).
- [12] T. P. Spiller, I. D'Amico, and B. W. Lovett, New J. Phys. **9**, 20 (2007).
- [13] S. Sahling, G. Remenyi, C. Paulsen, P. Monceau, V. Saligrama, C. Marin, A. Revcolevschi, L. Regnault, S. Raymond, and J. Lorenzo, Nature Phys. **11**, 255 (2015).
- [14] M. P. Estarellas, I. D'Amico, and T. P. Spiller, Phys. Rev. A **95**, 042335 (2017).
- [15] C. H. Bennett, G. Brassard, C. Crépeau, R. Jozsa, A. Peres, and W. K. Wootters, Phys. Rev. Lett. **70**, 1895 (1993).
- [16] R. Raussendorf and H. J. Briegel, Phys. Rev. Lett. **86**, 5188 (2001).
- [17] P. Walther, K. J. Resch, T. Rudolph, E. Schenck, H. Weinfurter, V. Vedral, M. Aspelmeyer, and A. Zeilinger, Nature **434**, 169 (2005).
- [18] A. K. Ekert, Phys. Rev. Lett. **67**, 661 (1991).
- [19] T. Jennewein, C. Simon, G. Weihs, H. Weinfurter, and A. Zeilinger, Phys. Rev. Lett. **84**, 4729 (2000).
- [20] C. H. Bennett, G. Brassard, and N. D. Mermin, Phys. Rev. Lett. **68**, 557 (1992).
- [21] A. Kay, arXiv preprint arXiv:1808.00696 (2018).
- [22] R. Bachman, E. Fredette, J. Fuller, M. Landry, M. Opperman, C. Tamon, and A. Tollefson, Quantum Information and Computation, **12**, 0293 (2012).
- [23] M. P. Estarellas, *Spin Chain Systems for Quantum Computing and Quantum Information Applications* (PhD thesis, University of York, York, 2018).
- [24] M. Christandl, N. Datta, A. Ekert, and A. J. Landahl, Phys. Rev. Lett. **92**, 187902 (2004).
- [25] A. Kay, Int. J. Quantum Inf. **8**, 641 (2010).
- [26] K. N. Wilkinson, M. P. Estarellas, T. P. Spiller, and I. D'Amico, Quantum Information and Computation **18**, 0247 (2018).
- [27] W. K. Wootters, Quantum Information and Computation **1**, 27 (2001).
- [28] R. Ronke, T. P. Spiller, and I. D'Amico, Phys. Rev. A **83**, 012325 (2011).

APPENDIX: EOF NEAR COUPLING RATIO

$$\frac{\delta}{\Delta} = 0.504469524022$$

In Fig. 11 the behavior of the time of the first *EOF* peak around a minimum of the orange dashed curve in Fig. 10 is shown. In this graph, the time, t_E , seems to reach a maximum of $t_E \cdot \Delta = 4000$ for ratios near to $\frac{\delta}{\Delta} = 0.504469524022$, this is in fact a consequence of the used simulation cutting off at this time. As the bottom left graph in Fig. 15 shows, systems with a coupling ratio in this region achieve their first maximum after $t_E \cdot \Delta = 4000$ (although the highest *EOF* in the considered time range is just before $t_E \cdot \Delta = 4000$). Figure 15 also offers an explanation for the multiple curves seen in Fig. 11: as the system exhibits periodic behavior, there are multiple *EOF* maxima for each coupling ratio. In Fig. 11 each curve corresponds to a different *EOF* maxima, which moves in time as the coupling ratio is changed. Due to the simulation used only choosing one maximum for each coupling ratio, the curves in Fig. 11 are not continuous, but in a true reflection of the time behaviour of the *EOF* maxima, there would be multiple points for each coupling ratio and each curve would therefore be continuous.

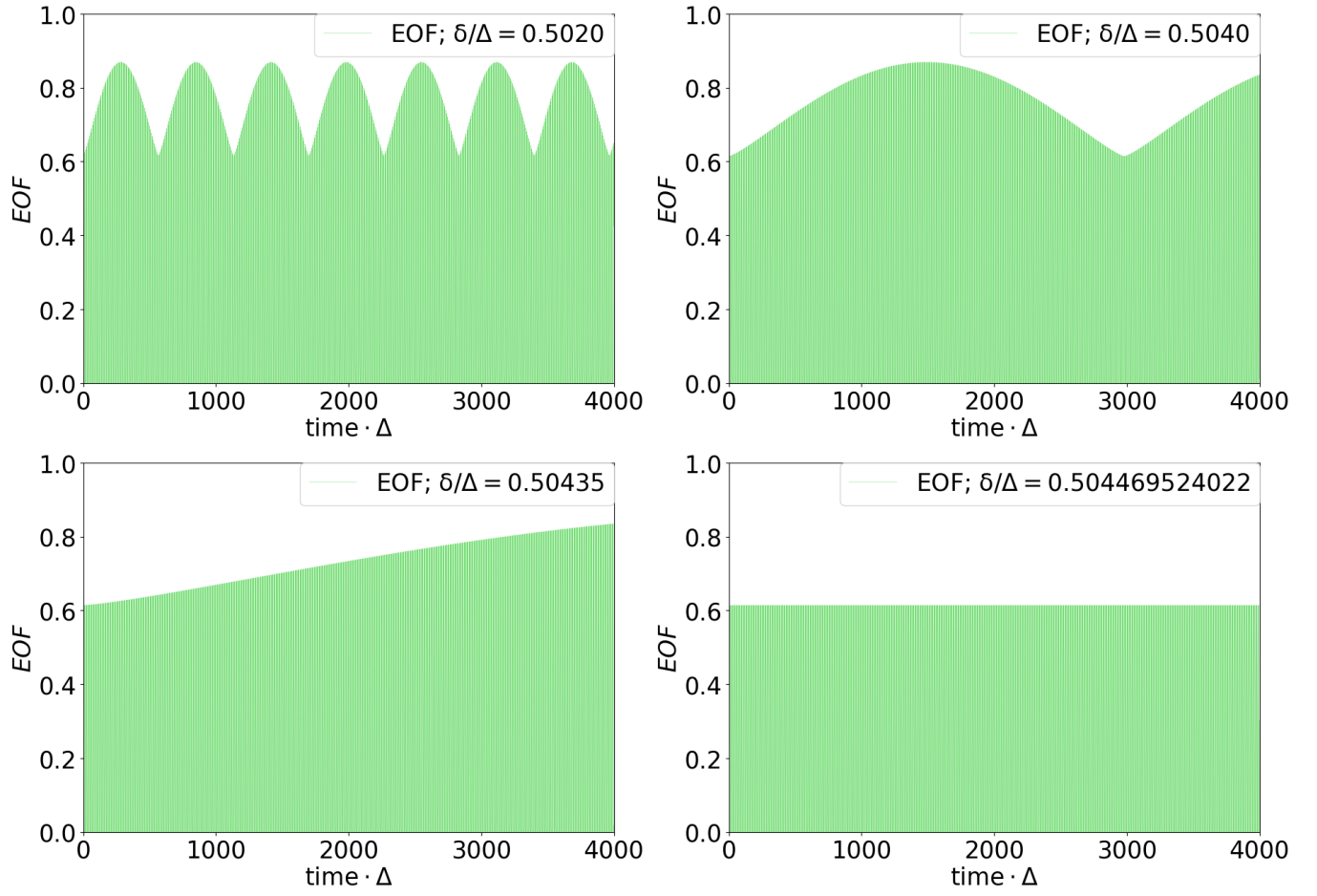


FIG. 15: EOF vs time for coupling ratio corresponding to the vertical red lines shown in Fig. 11. From top to bottom, left to right, the graphs show the EOF behaviour as the coupling ratio gets closer to the "flat ratio" $\frac{\delta}{\Delta} = 0.504469524022$. The top graphs show that for each coupling ratio there are multiple EOF maxima, and the bottom left graph shows that for ratios sufficiently close to the flat ratio, the first maximum will fall outside of the considered time window